Hindawi
Journal of Engineering
Volume 2023, Article ID 1457986, 14 pages
https://doi.org/10.1155/2023/1457986

Research Article

Computational Fluid Dynamics Simulation Assessment of Inlet Configuration Influence on Enhancing Swirl Flow Microbubble Generator Performance

Ali Al-Azzawi,[1] **Abouther Al-Shimmery**,[2] **Ahmed Alshara**,[1] **and Mohammed Razzaq Mohammed**[1]

[1]*Department of Mechanical Engineering, College of Engineering, University of Misan, Amarah, Iraq*
[2]*Department of Petroleum Engineering, College of Engineering, University of Misan, Amarah, Iraq*

Correspondence should be addressed to Ahmed Alshara; dr.ahmed_alshara@uomisan.edu.iq

Received 26 March 2023; Revised 26 August 2023; Accepted 7 September 2023; Published 26 September 2023

Academic Editor: Muhammed Hassan

In this study, a CFD simulation analysis was used to predict the characteristics of a swirl flow as a reference to optimize a new design of microbubble generator. To examine the impact of the inlet design, three different configurations of the inlet type were applied, namely single inlet, double inlet, and tangent-circle inlet. The performance of the microbubble generator was characterized in terms of swirl velocity, pressure drop in radial position, and pressure distribution along the central axis of the microbubble generator. Generally, the CFD analysis succeeded to visualize the hypothetical bath of the flow streamlines inside the microbubble generators. The results illustrated that the swirl flow in the tangent-circle inlet was able to generate a negative pressure zone in the central area of the generator (i.e., self-suction mechanism). In addition, the tangent-circle inlet showed a high-pressure drop compared with the single inlet microbubble generator. Although the double inlet microbubble generator illustrated a high-pressure drop between the inlet and the outlet, the streamlines distribution was focused only on the top part of the microbubble generator. This was a reason why the self-suction mechanism was not well defined.

1. Introduction

Microbubble-based technology has attracted a great deal of attention and has generally been developed to be a highly efficient green separation technology. Microbubbles, which are defined as a bubble with less than 100 μm in diameter [1], have unique characterizations; for instance, a large contact surface area per unit volume leads to an enhancement in heat and mass transfer phenomena, chemical reaction, and physical absorption between two phases (i.e., gas and liquid) [2–6]. As a result of these features, the use of microbubble technology has been introduced in many environmental and industrial processes such as water purification process [7] to improve water quality of polluted lakes and marshes [8], separation process of low-density droplets including separation oil from oily water [9], and medical therapeutic applications [7]. Several techniques can be applied to generate microbubbles, including porous membrane [10], Venturi-type [9], electrolysis and ultrasound [11], a constant flow-nozzle [12], a swirling jet flow [1], and pressurized dissolution method [13]. Among these techniques, many advantages are provided by using a microbubble generator that uses swirl flow, involving low cost and simple design with high performance to generate very small bubbles [14]. The following steps can describe the principles of the microbubble generator using swirl flow: downward vortices generated as a result of a tangent-circle inlet water flow from the top side of a cylindrical tank. This leads in generating a vacuum pressure in the central axis of the cylindrical tank which in turn causes suction of air from an orifice laying in the center bottom of the cylinder. Afterwards, the mixture discharges with water from a hole placed in the top base of the cylindrical tank [7, 15, 16]. Figure 1 demonstrates how the microbubble generator works.

Many studies have utilized the microbubble generator based on swirl flow; for example, Xu et al. [17] discussed the effect of the nozzle diameter on the gas self-suction, where the pressure at the gas inlet was detected by using different nozzle diameters. The results showed that increasing the geometric criterion K (i.e., $K = Dd_o/d_{in}^2$, where D is the inner diameter of the vortex chamber, d_o is the nozzle diameter, and d_{in} is the diameter of the liquid inlet) from 3.2 to 4.8 leads to an increase in the vacuum degree from zero to the maximum value. Takahashi et al. [15] conformed that the microbubbles having the peak of distribution around 25 μm in diameter can be formed using swirl flow. Alam et al. [18, 19] used unsteady numerical CFD simulation to visualize the characterization of the gas-liquid flow phenomenon in a dual chamber microbubble generator. According to the CFD results, the self-suction mechanism is clearly generated as a consequence of the swirl flow of liquid in the inner area of the vacuum chamber.

Despite the wide range of parameters investigated in the aforementioned studies, including the influence of the inlet diameter and a particular focus on conducting numerical simulations in the context of a dual chamber microbubble generator, there is currently a lack of comprehensive research investigating the impact of entrance geometry on the generation of vacuum zones.

However, designing a cost-effective and high-efficient microbubble generator for a wide range of applications is still a challenge [17, 19]. Therefore, the aim of this study is to investigate the effect of the different designs of the inlet of the microbubble generator on creating a low-pressure zone in the central area.

2. CFD Modeling

2.1. Physical Model. Figure 2 shows the three-dimensional model of the microbubble generator that was established by COMSOL Multiphysics based on the geometry developed by Xu et al. [17]. Table 1 illustrates the dimensions of the microbubble generator.

Three suggested designs have been utilized in this study as follows: single inlet, double inlet with opposite direction, and tangent-circle inlet as shown in Figures 3 and 4.

2.2. Computational Model. To solve the water flow problems over the cylindrical surface of the microbubble generator, a turbulent flow of a single-phase model was used. Among all the turbulent flow models that were provided by COMSOL Multiphysics software, v2-f turbulent model is applied in this study. It is an extension of the k-ε turbulence model and according to the release notes for update version 5.3 of COMSOL Multiphysics, the v2-f turbulence model can be used to describe the flow over the curved surface, where this model can provide a high accuracy over the other turbulence models [20]. In addition, for hydrocyclone, which is the closest model to this study, COMSOL Multiphysics had used v2-f turbulence model as a suitable model to describe the swirl flow [21]. The main feature of this model is the capability of providing the required calculations of the flow occurring within the whole thickness of the boundary layer. The v2-f turbulent model is denoted as a low-Reynolds number model which can solve the Navier–Stokes equations and the continuity equation for both momentum and mass conservation laws [22].

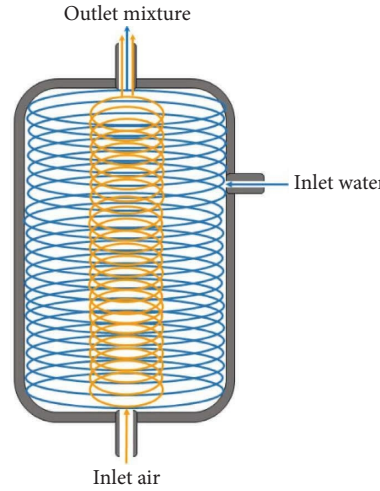

Figure 1: Schematic diagram of the microbubble generator flow principle.

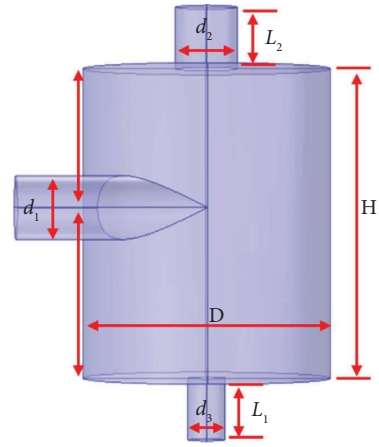

Figure 2: Schematic illustration of the dimensions of the microbubble generator [17].

Table 1: Dimensions of the microbubble generator.

Symbol	Parameter	Value (mm)
H	Height	25
D	Diameter	20
L_1	Inlet height	5
L_2	Outlet height	5
d_1	Inlet diameter	5
d_2	Outlet 1 diameter	5
d_3	Outlet 2 diameter	5

The incompressible Navier–Stokes equation is as follows:

$$\rho(\mathbf{u}.\nabla)\mathbf{u} = \nabla.[p\mathrm{I} + \mathrm{K}] + F. \quad (1)$$

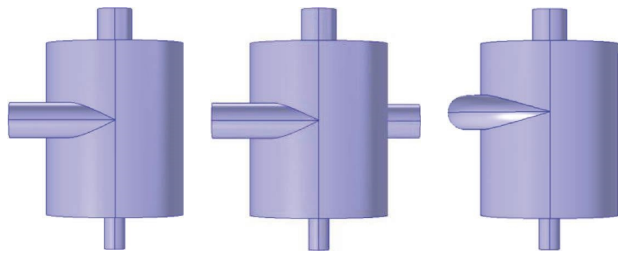

Figure 3: Side view of microbubble generators: (a) single inlet, (b) double inlet, and (c) tangent-circle inlet.

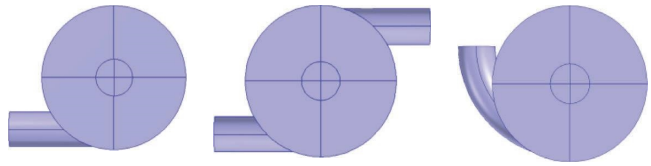

Figure 4: Top view of microbubble generators: (a) single inlet, (b) double inlet, and (c) tangent-circle inlet.

The continuity equation is as follows:

$$\rho \nabla . \mathbf{u} = 0, \tag{2}$$

where $\boldsymbol{\rho}$ is the fluid density, $\mathbf{p}$ is the pressure, $\mathbf{u}$ is the fluid velocity, ∇ is the Nabla operator, $\mathbf{F}$ is the vector field of mass forces, $\mathbf{I}$ is the intensity of the turbulent flow, and vector $\mathbf{K}$ is calculated as the product of the sum of viscosities (dynamic and turbulent) and velocity operators as follows:

$$K = \left(\mu + \mu_T\right)\left(\nabla \mathbf{u} + (\nabla \mathbf{u})^T\right)0, \tag{3}$$

where μ is the dynamic viscosity and μ_T is the turbulent dynamic viscosity.

In v2-f model [22, 23], which introduces two equations, the first equation explains the movement of turbulence perpendicular to the wall through a variable represented by $(\zeta = \overline{u^2}/k)$. The symbol $\overline{u^2}$ represents the variance of the turbulent velocity's normal component, meanwhile k denotes the turbulence kinetic energy. The second equation is an elliptic partial differential equation used for determining the blending coefficient (α). This elliptic blending equation takes into consideration nonlocal effects, including the dampening of turbulence kinetic energy redistribution between the parallel and normal directions caused by the wall. Thus, the complete model can be written as follows:

$$\begin{aligned}
\rho(\mathbf{u}.\nabla)k &= \nabla.\left[\left(\mu + \frac{\mu_T}{\sigma_k}\right)\nabla k\right] + P_k - \rho_\epsilon,\\
\rho(\mathbf{u}.\nabla)\epsilon &= \nabla.\left[\left(\mu + \frac{\mu_T}{\sigma_\epsilon}\right)\nabla \epsilon\right] + \frac{1}{\tau}\left(C_{\epsilon 1}^{'}(\zeta,\alpha)P_k - C_{\epsilon_2}^{'}(k,\epsilon,\alpha)\rho_\epsilon\right),\\
\rho(\mathbf{u}.\nabla)\zeta &= \nabla.\left[\left(\mu + \frac{\mu_T}{\sigma_\zeta}\right)\nabla \zeta\right] + \frac{2}{k}\left(\alpha^3\mu + \frac{\mu_T}{\sigma_k}\right)\nabla k.\nabla\zeta + \left(1-\alpha^3\right)f_w + \alpha^3 f_h - \frac{\zeta}{k}P_k,
\end{aligned} \tag{4}$$

where ζ is the turbulent relative fluctuations, α is the elliptic blending function alpha, ϵ is the turbulent dissipation rate, α is the elliptic blending function, and σ is the stresses in the fluid flow.

The v2-f model presents two principles, the first concept (i.e., turbulence generation (P_k)) is depicted in the following equation:

$$P_k = \mu_T\left[\nabla \mathbf{u}\colon \left(\nabla \mathbf{u} + (\nabla \mathbf{u})^T\right)\right]. \tag{5}$$

The significance of this concept in physical terms lies in the creation of vortices and ripples, which make up the turbulence. The second notion involves the turbulent dispersion rate (ϵ), which represents the transforming vortices from a larger size to a smaller one; this process results in a reduction in turbulence. The elliptic mixing function α, which correlates with the length of turbulence, can be expressed in the following form:

$$\alpha - L^2\nabla^2\alpha = 1, \tag{6}$$

where L is the turbulence length, which can be expressed in the following equation:

$$L = C_L \max\left[\frac{k^{(3/2)}}{\epsilon}, C_\eta\left(\frac{\nu^3}{\epsilon}\right)^{1/4}\right], \quad (7)$$

where ν is the kinematic viscosity.

2.3. Mesh Generation and Boundary Condition Setup. The grid models of the different inlets of the microbubble generators are shown in Figure 5. The option "physics-induced sequence" was used to generate the computational mesh. It is a physical control mesh, where it can automatically create a mesh according to what is required in the physical interface of the studied model. It depends on three main features, which are physical property setting (i.e., finer mesh for the turbulence model than a laminar flow), certain feature (i.e., finer mesh for walls with boundary layer meshes), and geometry bounding box size (i.e., control the size of the elements) [21, 24]. The physics-controlled meshing sequence for this study includes the subnodes, which are coarse mesh for the size which depends on the property settings and the bounding box of the geometry; fine mesh (size 1) for all no-slip walls; finer mesh (corner refinement 1) used to decrease the element size at sharp corners, free tetrahedral 1 to construct a mesh for the remaining regions, boundaries, edges, and individual points; and boundary layers 1 applied to create a dense mesh and long no-slip walls.

The following considerations have been used: the problem of the fluid flow is a steady state, single phase, Newtonian, and incompressible fluid (water, density = 1000 kg/m3, viscosity = 0.00102 *Pa.s*). The inlet is set as a velocity (i.e., normal inflow velocity) at 1–4 m/s. A no-slip condition (i.e., the velocity value is zero on the wall) was applied for all walls. The overflow and underflow outlets were defined with the boundary condition of pressure (i.e., atmospheric pressure).

3. Results and Discussion

Figures 6(a) and 6(b) show the horizontal and vertical lines where the swirl velocity, pressure gradient, and pressure distribution graphs are determined, respectively. Meanwhile, Figures 6(c) and 6(d) display a plane where the surface pressure and velocity streamlines were drawn.

3.1. Swirl Velocity. Four different inlet velocities (1, 2, 3, and 4 m/s) were studied to examine the influence of the inlet velocity on the swirl velocity. The swirl velocity was calculated using the following equation (21):

$$\text{swirl velocity} = \frac{(x \times v - y \times u)}{\sqrt{x^2 + y^2 + \text{eps}}}, \quad (8)$$

where u and v velocity field components in x and y coordinates, respectively, and eps is a very small nonzero term (machine epsilon).

Figure 7 displays the swirl velocity as a function of the radial position for each geometry. In single inlet microbubble generator, the graph is not fully axisymmetric. Meanwhile, a symmetric graph can be achieved around the center region of the double inlet and tangent-circle inlet generators. Generally, the same trend was noticed for the three microbubble generators, where the swirl velocity increased sharply to reach the maximum value somewhere on the radius and then decreased gradually to become close to zero at the center line.

For quantity comparison, from Figure 7, the double inlet microbubble generator exhibited a twofold increase in the swirl velocity compared to the swirl velocity of the single inlet microbubble generator. For example, when the inlet velocity was 1 m/s, the swirl velocity of the single inlet microbubble generator was 0.956 m/s, whereas the swirl velocity was 1.761 m/s for the double inlet microbubble generator. On the other hand, the tangent-circle inlet microbubble generator displayed around one-fold and half increase in the swirl velocity. For instance, when the inlet velocity was 1 m/s, the swirl velocity of the single inlet microbubble generator was 0.956 m/s. In the meantime, the swirl velocity was 1.36 m/s for the tangent-circle inlet microbubble generator. Table 2 shows the influence of the inlet velocity on the swirl velocity for different types of microbubble generators.

3.2. Velocity Streamline. Generally, the swirl velocity distribution for the three microbubble generators is nearly identical in pattern. From the contour plots of the swirl velocity (Figure 8), the following comments can be said. Two regions can be recognized, which are an inner region and an outer region. In the inner region, the swirl velocity decreased sharply until reaching the minimum value at the center line. Meanwhile, in the outer region, the swirl velocity increased with a radius until reaching the inner wall of the microbubble generators. To compare between the generators, it observed from Figure 8 that the intensity or high shearing rate on the wall of the double inlet generator is higher than that of the other generators. However, the distribution of the shearing rate in the double inlet generator is not homogenous. It focuses only in the upper part of the generator. Meanwhile, the distribution of the shearing rate is homogenous in all parts of the tangent-circle inlet microbubble generator.

In order to investigate the circulation flow in the microbubble generators, a 3D view was used to show the streamlines of the swirling flow inside the microbubble generators. Generally, the flow circulations are directly affected by inlet velocity; higher the inlet velocity, higher the flow circulations. Furthermore, it can be seen from Figure 9 that the forward motion was close to the wall of the microbubble generators. Meanwhile, the reverse motion was along the center line of the microbubble generators.

The main reason of the counter flow phenomenon is the negative pressure that generated in the central axis of the microbubble generator. On the other hand, it is worth pointing that this phenomenon had been confirmed by many experimental and CFD simulation studies [17–19, 24].

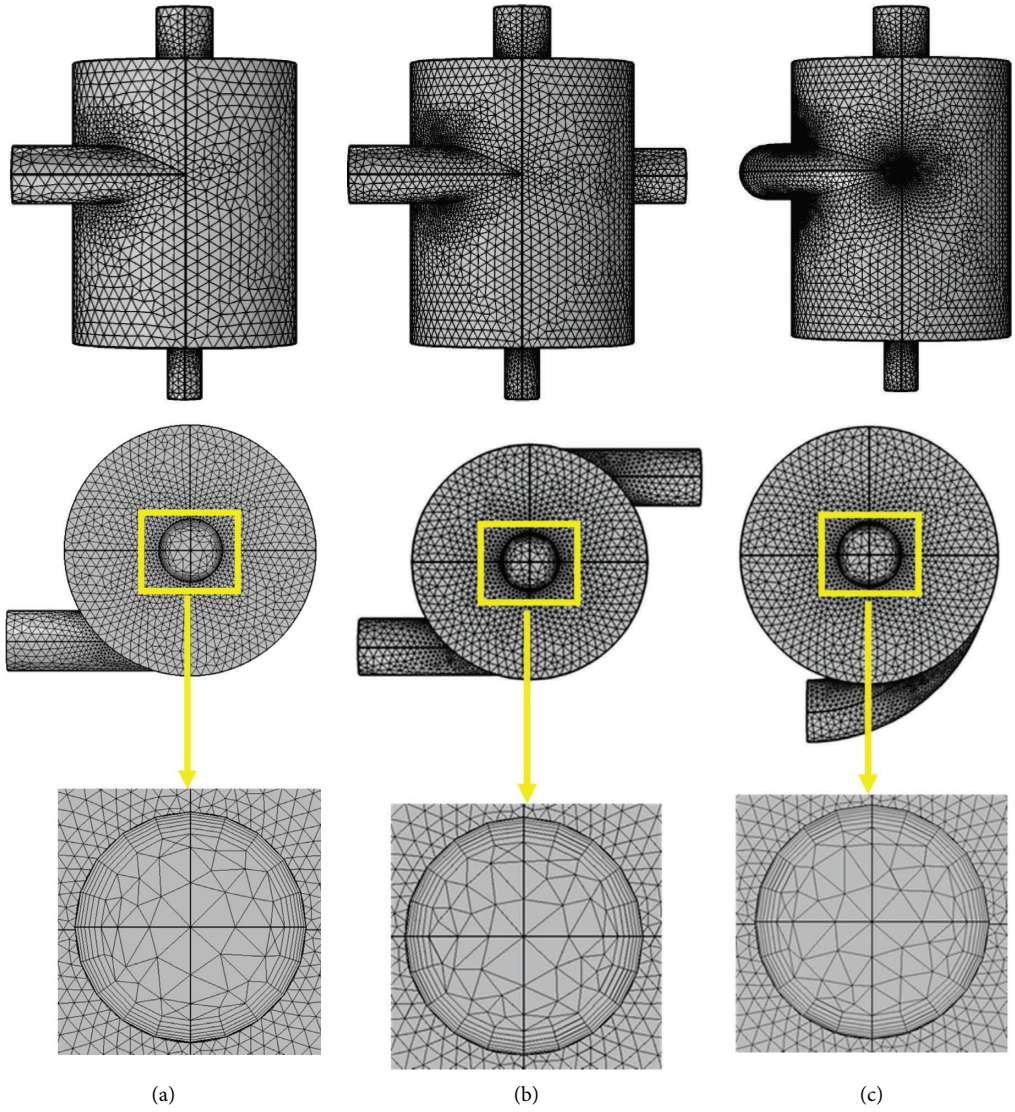

Figure 5: Grid models of the microbubble generators: (a) single inlet, (b) double inlet, and (c) tangent-circle inlet.

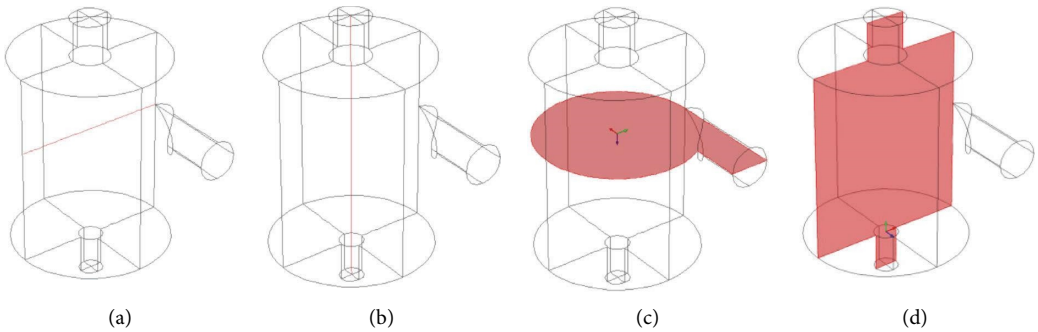

Figure 6: The position where the results are taken: (a) cut line 3D at z-coordinate = 15 mm, (b) cut line 3D at y-coordinate = 0, (c) y-x plane at z-coordinate = 15 mm, and (d) x-z plane at y-coordinate = 0.

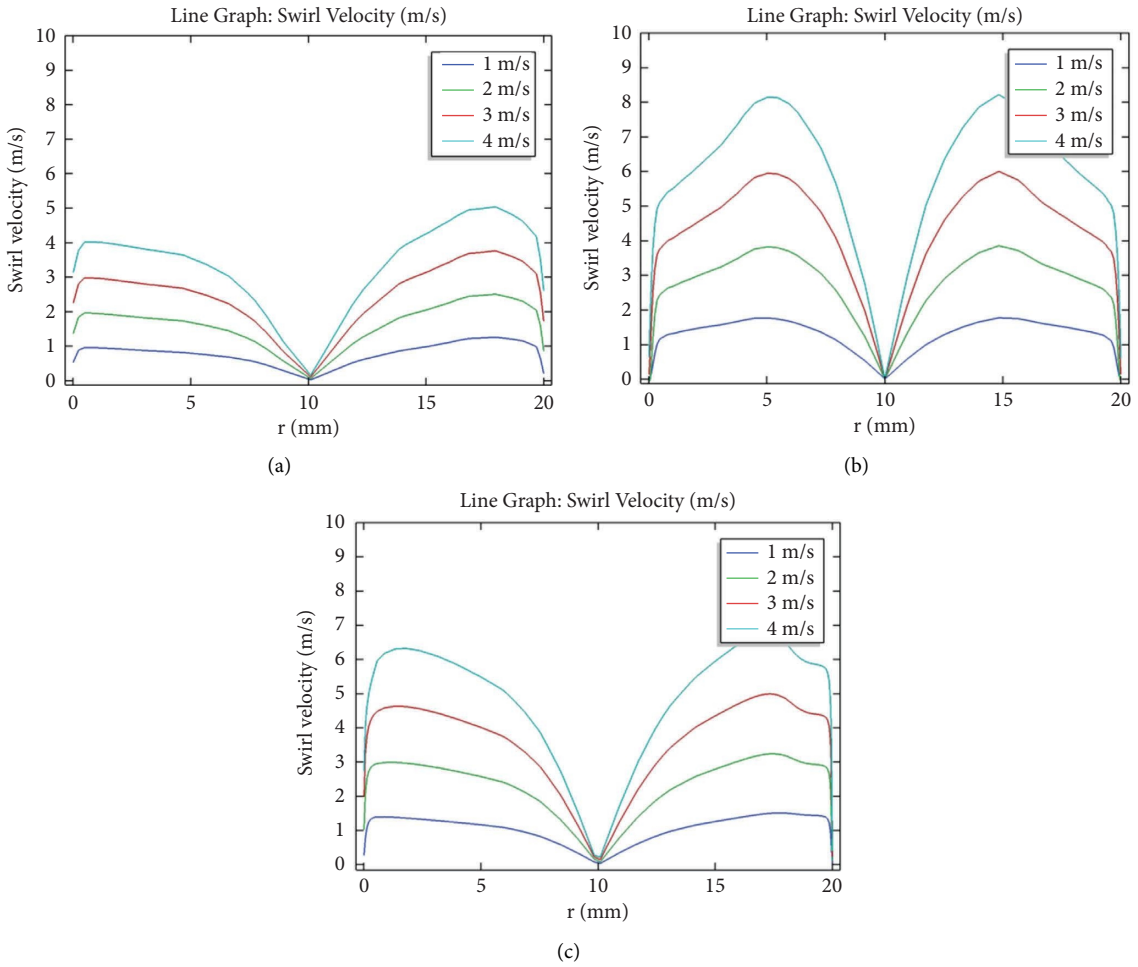

Figure 7: Swirl velocity at different inlet velocities: (a) single inlet, (b) double inlet, and (c) tangent-circle inlet.

Table 2: The influence of the inlet velocity on the swirl velocity.

Type	Inlet velocity (m/s)	Position from left to right (mm)	Maximum swirl velocity
Single inlet	1	0.48283	0.956296
	2	0.48283	1.957903
	3	0.48283	2.977925
	4	0.48283	4.017543
Double inlet	1	5.018579	1.761682
	2	5.018579	3.819073
	3	5.018579	5.943624
	4	5.018579	8.14321
Tangent-circle inlet	1	1.649087	1.361161
	2	1.649087	2.964799
	3	1.649087	4.594135
	4	1.842395	6.250447

To compare quantitatively between the microbubble generators, for the single inlet and the tangent-circle inlet, the flow can reach all parts of the microbubble generators (i.e., upper part and lower part). Conversely, for the double inlets, Figure 9 shows that the flow could not reach the lower face of the generator and concentrated at the upper part of the microbubble generator.

It also confirms the circulation flow from Figure 10, where it shows the velocity vectors of fluid flow in a parallel plane of the inlet section. The high intensity of the arrow volume of the velocity field starts from the inner wall of the microbubble generator until reaching the low-pressure zone for both the single inlet and tangent-circle inlet microbubble generators. On the other hand, in the double inlet

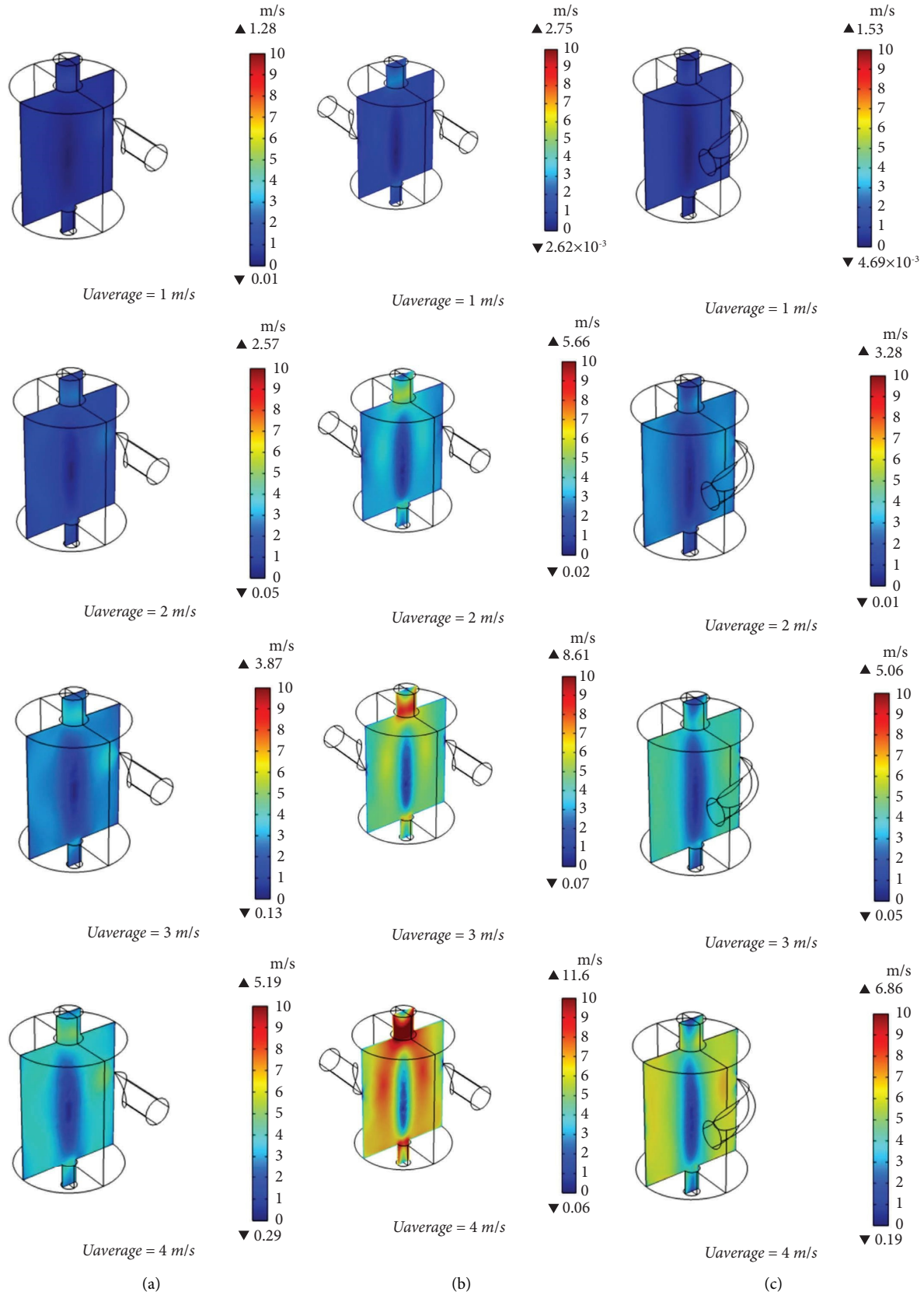

FIGURE 8: Spatial distribution of swirl velocities at different inlet velocities: (a) single inlet, (b) double inlet, and (c) tangent-circle inlet.

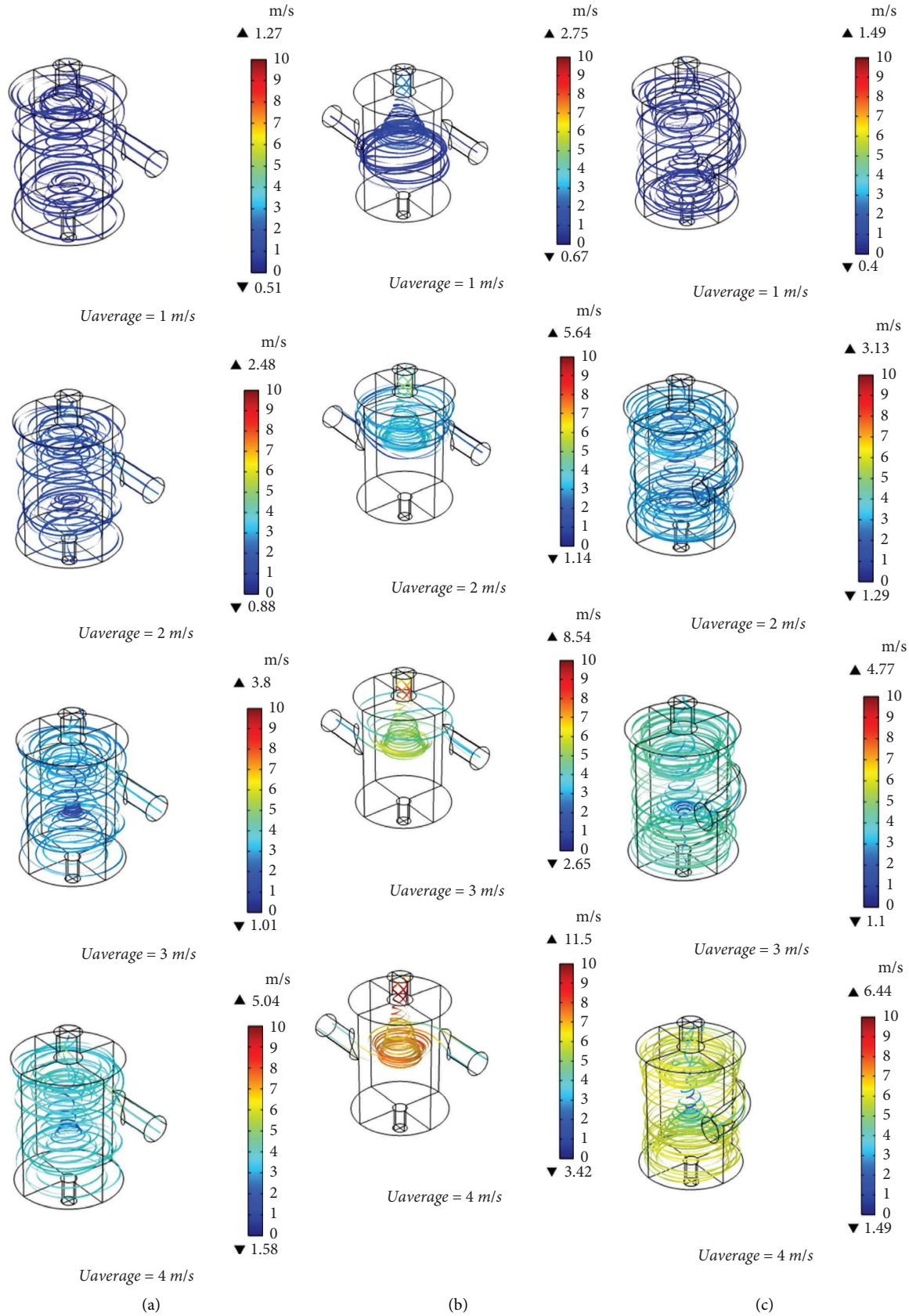

Figure 9: Velocity streamlines at different inlet velocities: (a) single inlet, (b) double inlet, and (c) tangent-circle inlet.

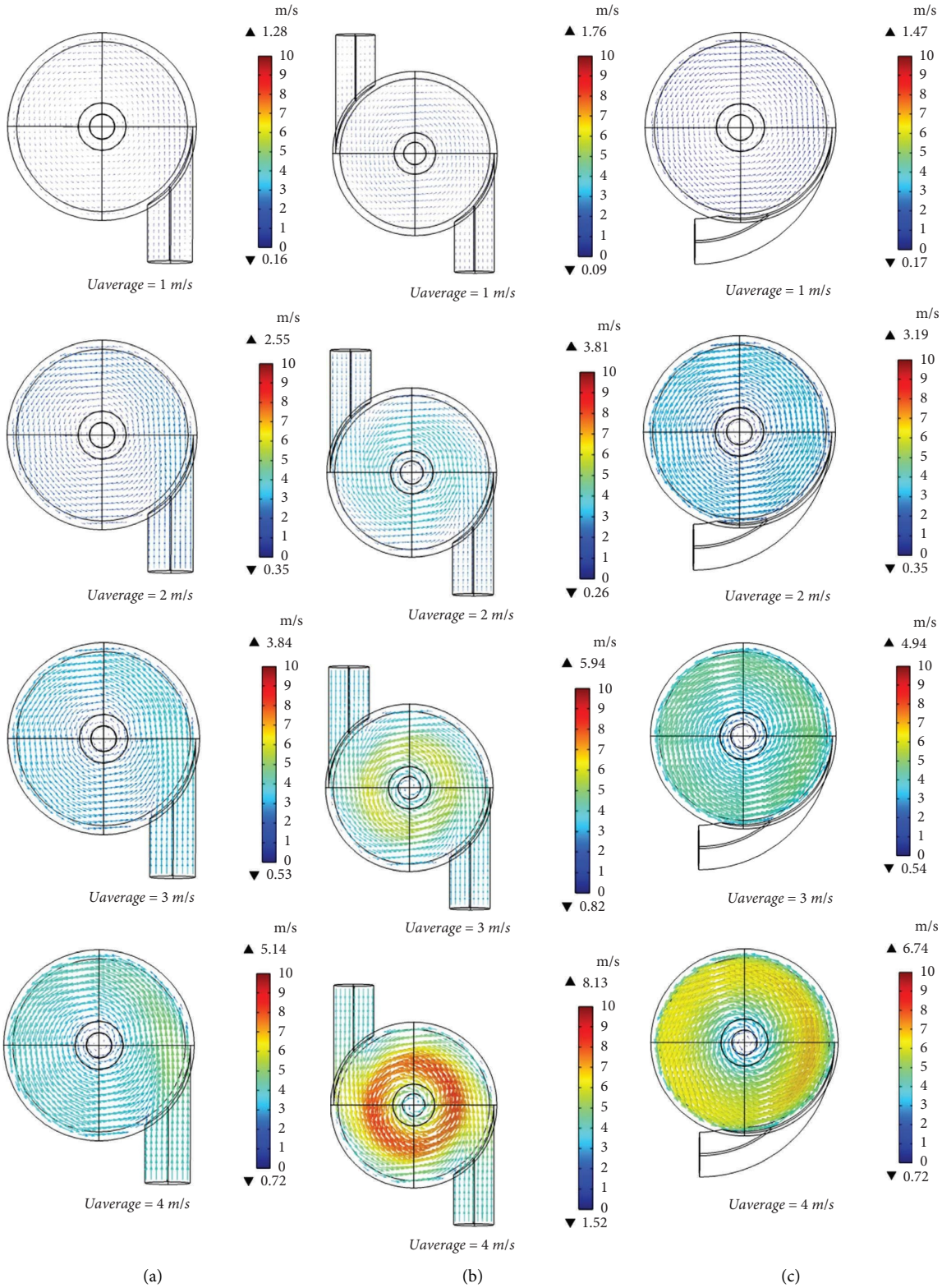

Figure 10: Velocity field at different inlet velocities: (a) single inlet, (b) double inlet, and (c) tangent-circle inlet.

microbubble generator, the arrow volume of the velocity field concentrated in a small area around the low-velocity zone due to the effect of the double inlet generator.

3.3. Pressure Drop. Pressure distribution inside the microbubble generators is investigated, and the results are illustrated in Figure 11 where they show the pressure profile for

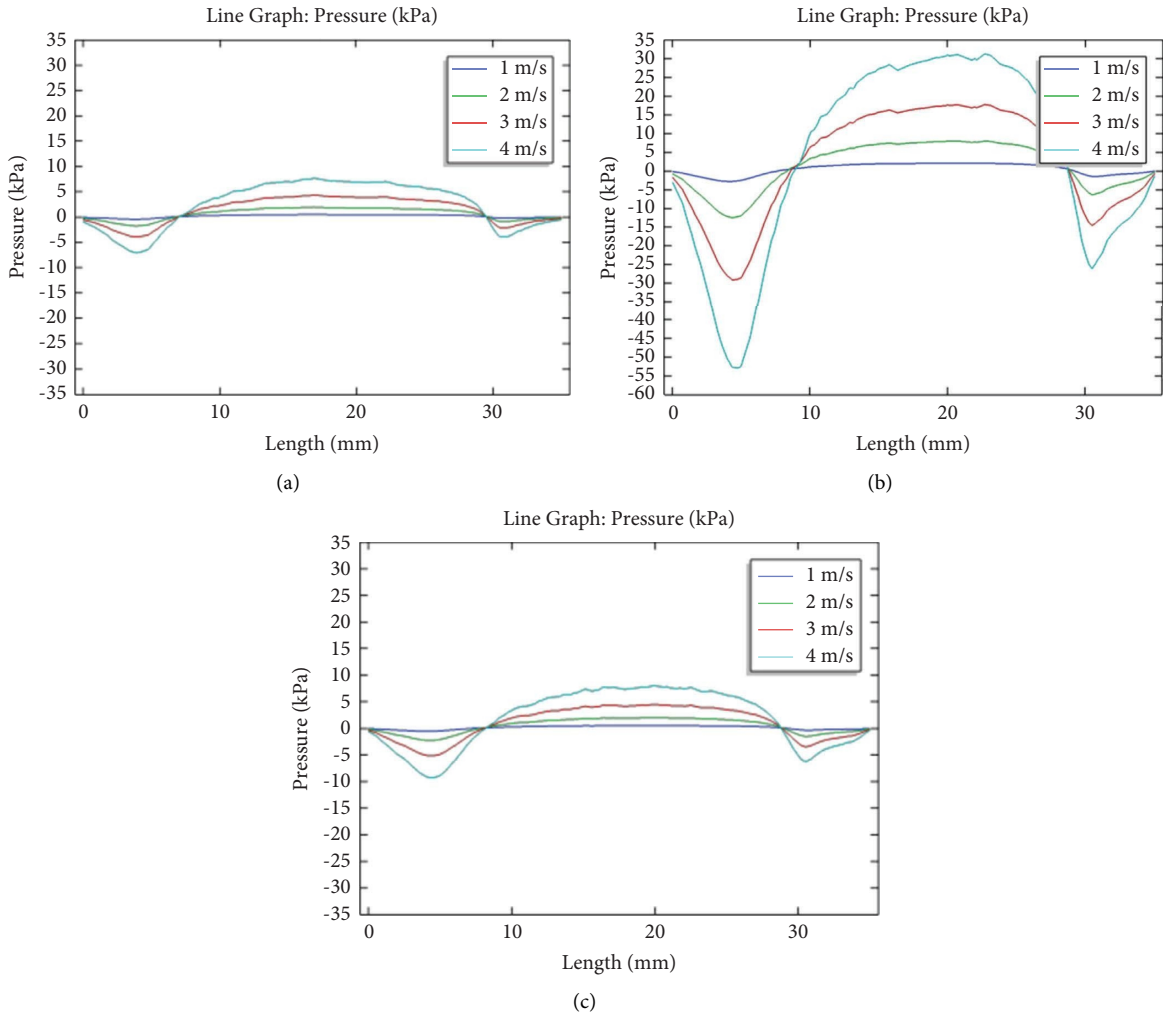

Figure 11: Pressure distribution at different inlet velocities: (a) single inlet, (b) double inlet, and (c) tangent-circle inlet.

each geometry as a function of its length at velocities 1–4 m/s. The pressure distribution for each case is generally the same as it can be seen from Figure 11, where the graph clearly shows three different pressure magnitude regions. The vacuum pressure was generated at the lower region (i.e., the underflow outlet (0–5 cm)), while the high pressure appeared to be on the wall of the middle region (i.e., the central part of the generator (5–30 cm)). The main reason can be explained by the tangent-circle inlet velocity, which increases as a result of increasing the inlet velocity which in turn results in the increase of the turbulent kinetic energy, consequently, leading to produce high pressure [25, 26]. The intensity of the swirl flow is obviously dependent on the inlet velocity and the design of the generator. As it can be seen from Figure 11, the intensity increased gradually with an increase in the inlet velocity for all types of microbubble generators. Finally, in the overflow region, which includes the overflow outlet (30–35 cm), vacuum pressure can also be detected. The negative pressure value of the overflow and underflow increased continuously as the inlet velocity increase, and the underflow negative pressure is slightly higher than the overflow in the beginning. However, the difference became larger as the inlet velocity increased. This results in the form of the low-pressure zone. The liquid stream is pumped tangentially into the central part of the microbubble generator (i.e., the swirl chamber), leading to generate a high-speed swirl motion. This consequently leads to creating a low-pressure zone along the center line of the microbubble generator (for better understanding see Figure 12 that shows the low-pressure zone).

To compare between the different microbubble generators, an irregular configuration of a low-pressure zone (in the center line of the microbubble generator) with the tangent-circle inlet microbubble generator can be displayed in Figure 13 which is represented by the blue area or low pressure. Furthermore, the low-pressure zone initially developed at 1 m/s and gradually became stabilized, clear, and continuous for the entire microbubble generator while increasing the inlet velocity from 1 to 4 m/s. It can also be noticed that this configuration had regular shapes for both lower and upper outlets compared with the central part of the microbubble generator. The pressure contours of the three different

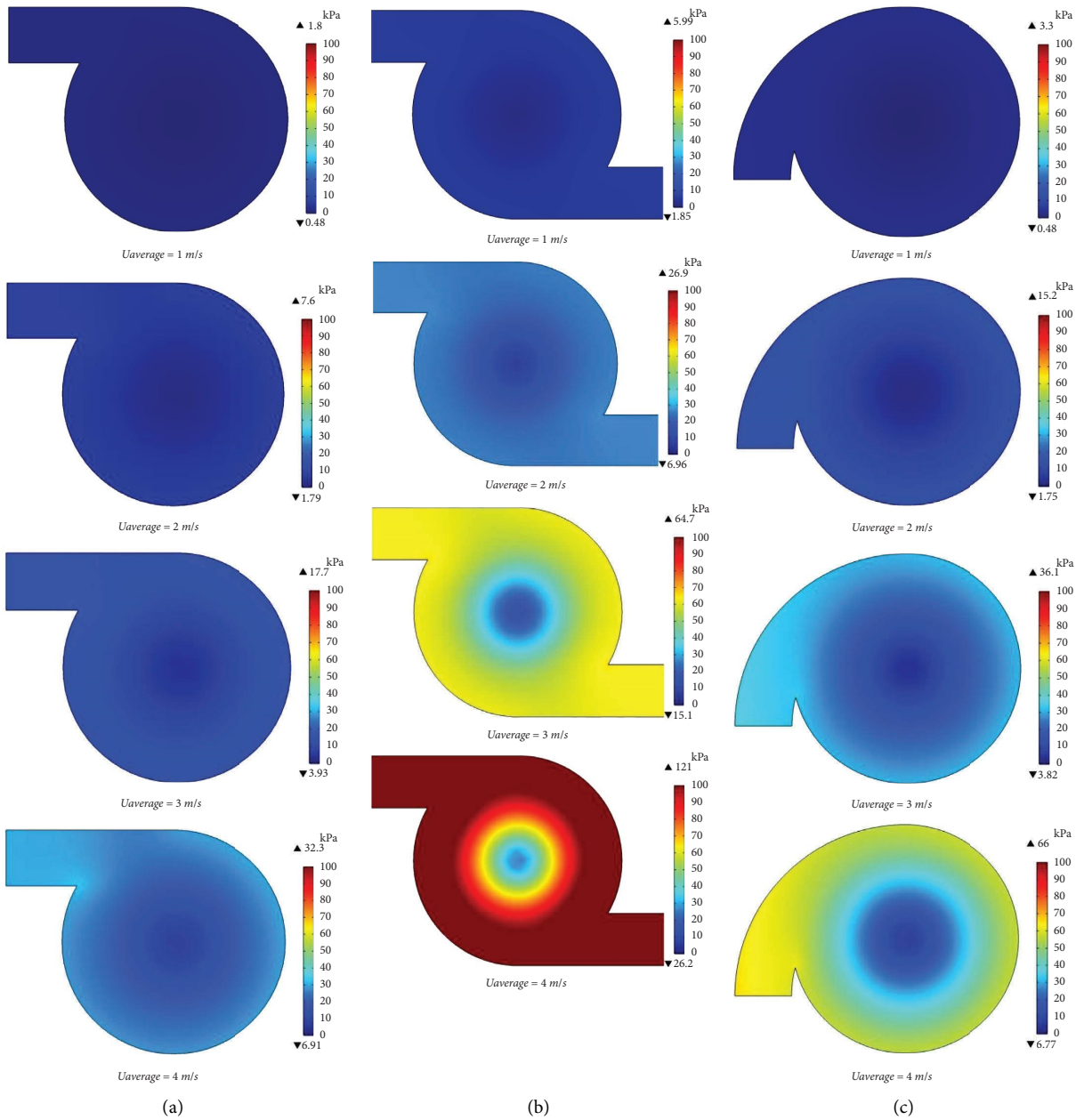

Figure 12: Gradient pressure contours at different inlet velocities: (a) single inlet, (b) double inlet, and (c) tangent-circle inlet.

geometries are shown in Figure 12. The blue area (i.e., core or vacuum area), particularly in the tangent-circle inlet geometry, became clearly visible compared to the other models.

This phenomenon mainly happened as a result of a low-pressure region developed along the center line of the microbubble generator. Figure 14 illustrates the characteristic of the pressure gradient over a diameter line at different inlet velocities. Generally, the pressure gradient increased with an increase in the inlet velocity for all types of the microbubble generators. The maximum value of pressure rose at the wall, whereas the minimum value appeared at the center line. In addition, it can be seen from Figures 7 and 14 that there is a correlation between the pressure drop and the gradient of the swirl velocity in the radial direction. This explained that the pressure gradients and the centrifugal forces are equal to each other (i.e., the higher the pressure gradient, the higher the velocity gradient) [27].

Pressure drop can also be an indicator to determine the operation cost for different geometry designs of the microbubble generators. Therefore, the differences between the static pressure at the inlet and outlet were applied to calculate the pressure drop. Table 3 shows the pressure drop of various microbubble generators. The results indicated that the maximum pressure drop can be obtained by the double inlet microbubble generator. The pressure drop is equal to 116.95, 62.23, and 29.68 kPa at 4 m/s as an inlet velocity for double inlet, tangent-circle inlet, and single inlet generators, respectively. It can be concluded from Figure 14 that the

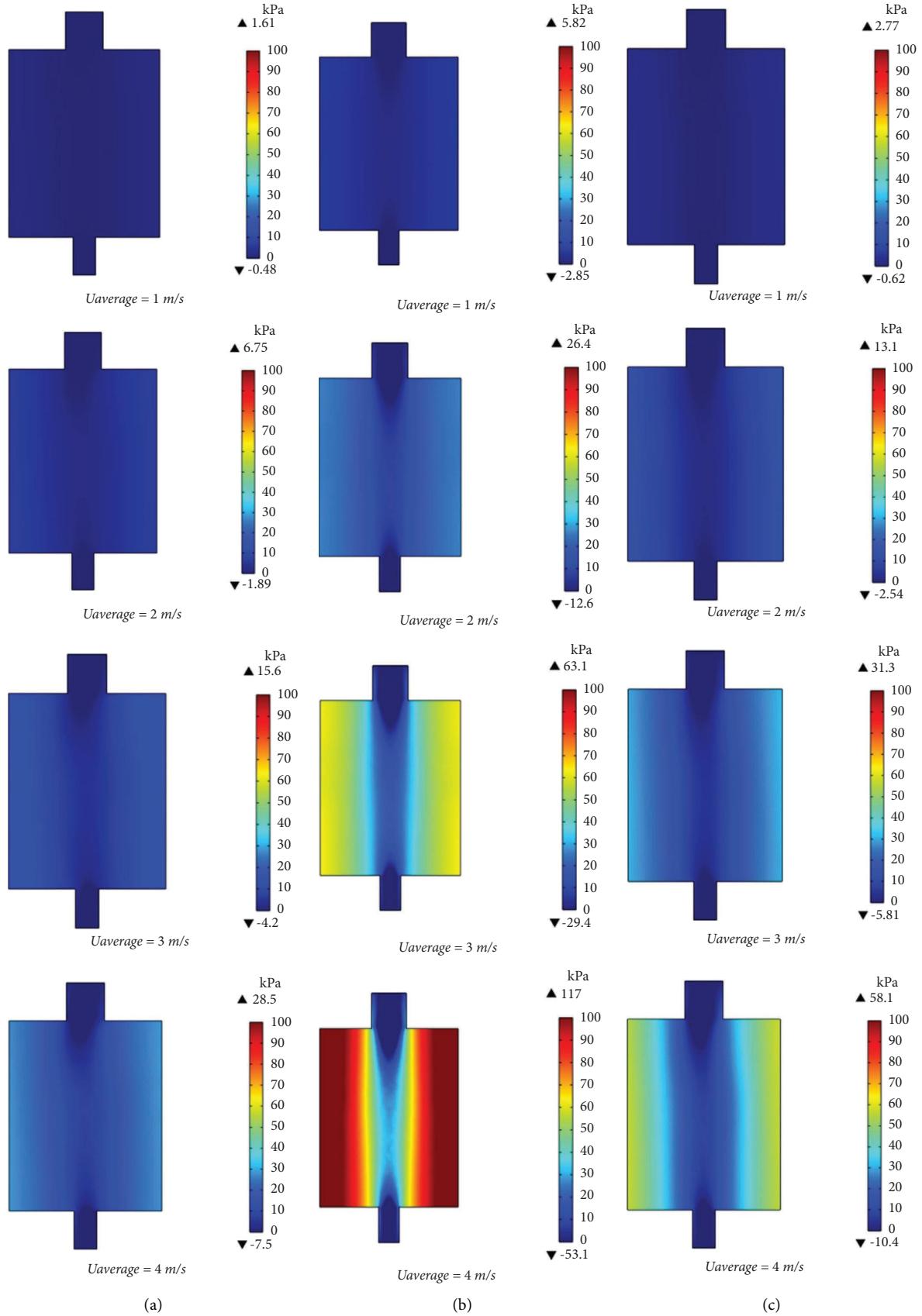

Figure 13: Pressure contours at different inlet velocities: (a) single inlet, (b) double inlet, and (c) tangent-circle inlet.

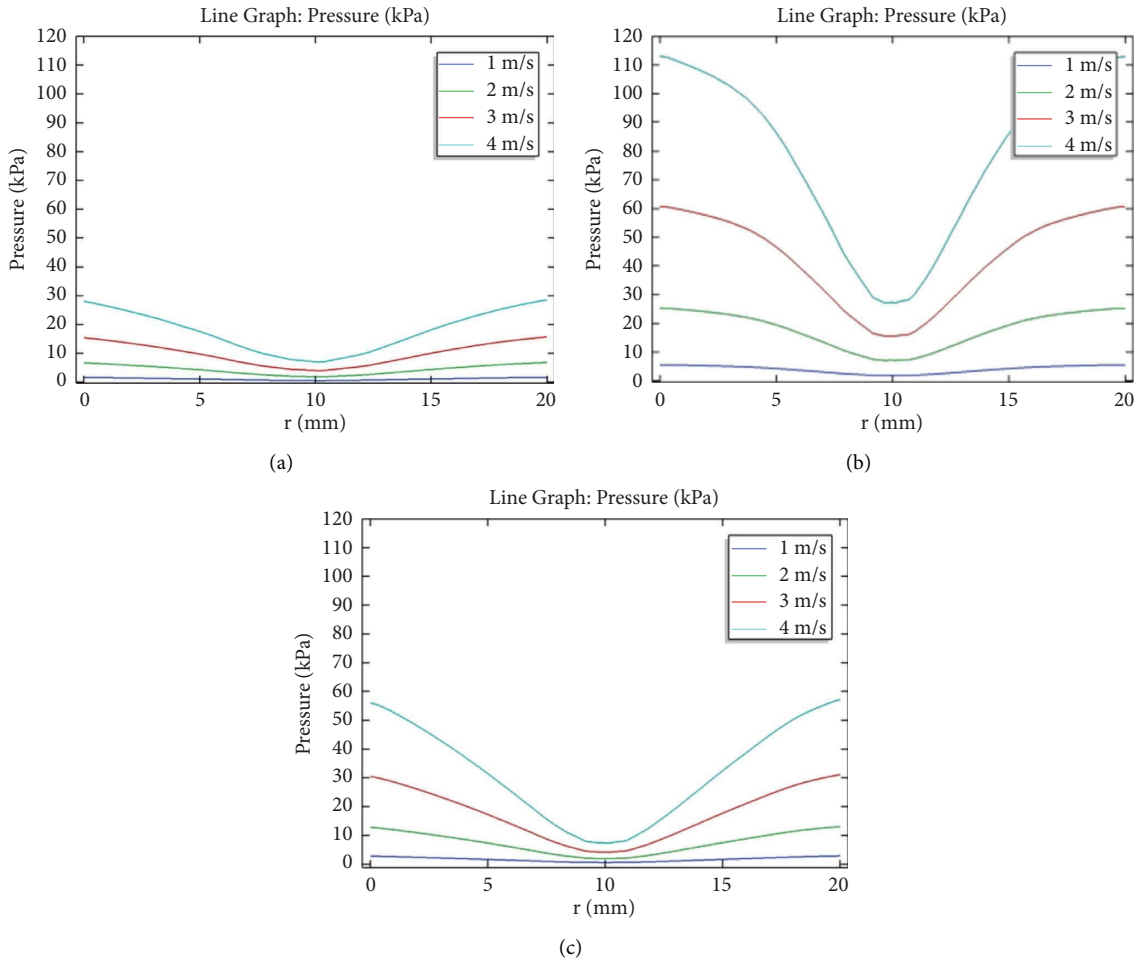

Figure 14: Pressure gradient at different inlet velocities: (a) single inlet, (b) double inlet, and (c) tangent-circle inlet.

Table 3: The pressure drop of different inlet-type microbubble generators.

Inlet velocity (m/s)	Pressure drop (kPa)		
	Single inlet	Double inlet	Tangent-circle inlet
1	1.71	5.86	3.08
2	7.08	26.31	14.29
3	16.31	62.88	33.96
4	29.68	116.95	62.23

pressure distributed systematically along the center line of all microbubble generators and gradually increased from inside to outside. The differences between the generators have clearly appeared for single and double inlet microbubble generators; the low-pressure zone (i.e., the central area or the blue area) is not well defined and the vacuum pressure concentrated only at overflow and underflow outlets areas. Meanwhile, in the tangent-circle inlet, the low-pressure zone was formed and continued from the bottom to top.

4. Conclusions

To explore the influence of the inlet design on the formation of the self-suction phenomenon in the swirl flow microbubble generator, a CFD simulation study was performed using COMSOL Multiphysics by employing the v2-f turbulent flow model interface. Three different inlet designs of the microbubble generators, which are single inlet, double inlet, and tangent-circle inlet, were investigated in this study. Generally, the CFD simulation results indicate that the vacuum zone (i.e., low-pressure zone) in the central area of the three microbubble generators was successfully formed as a result of the swirl flow of the fluid in the main body of the generator.

However, the low-pressure zone was clear and well defined with cylindrical shape in the tangent-circle inlet microbubble generator. Meanwhile, the low-pressure zone is not clear in the single inlet microbubble generator, and for the double inlet microbubble generator, the low-pressure zone is not well defined with a clear narrow area in the center of the microbubble generator.

The CFD simulation showed a strong ability to visualize the hydrodynamic flow in precise detail through the microbubble generator. However, there is a need to validate the CFD results with experiments because the friction loss between fluid and the internal structure of the microbubble generator was not taken into consideration.

Data Availability

The research data used to support the findings of this study are included within the article.

Conflicts of Interest

The authors declare that they have no conflicts of interest.

References

[1] K. Tabei, S. Haruyama, S. Yamaguchi, H. Shirai, and F. Takakusagi, "Study of micro bubble generation by a swirl jet (measurement of bubble distribution by light transmission and characteristics of generation bubbles): (measurement of bubble distribution by light transmission and characteristics of generation bubbles)," *Journal of Environment and Engineering*, vol. 2, no. 1, pp. 172–182, 2007.

[2] R. Parmar and S. K. Majumder, "Microbubble generation and microbubble-aided transport process intensification—a state-of-the-art report," *Chemical Engineering and Processing: Process Intensification*, vol. 64, pp. 79–97, 2013.

[3] S. Burns, S. Yiacoumi, and C. Tsouris, "Microbubble generation for environmental and industrial separations," *Separation and Purification Technology*, vol. 11, no. 3, pp. 221–232, 1997.

[4] T. Numakura, K. Kashiwagura, and T. Makuta, "Development and optimization of a microbubble generator with a hollow cylindrical ultrasonic horn," *Journal of the Japanese Society for Experimental Mechanics*, vol. 14, pp. s52–s56, 2014.

[5] S.-Y. Jeon, J.-Y. Yoon, and C.-M. Jang, "Bubble size and bubble concentration of a microbubble pump with respect to operating conditions," *Energies*, vol. 11, no. 7, p. 1864, 2018.

[6] A. Gurung, O. Dahl, and K. Jansson, "The fundamental phenomena of nanobubbles and their behavior in wastewater treatment technologies," *Geosystem Engineering*, vol. 19, no. 3, pp. 133–142, 2016.

[7] S. Khuntia, S. K. Majumder, and P. Ghosh, "Microbubble-aided water and wastewater purification: a review," *Reviews in Chemical Engineering*, vol. 28, no. 4-6, pp. 191–221, 2012.

[8] S. Oshita and T. Uchida, "Basic characterization of nanobubbles and their potential applications," *Bio-Nanotechnology: A Revolution in Food, Biomedical and Health Sciences*, Wiley, Hoboken, NY, USApp. 506–516, 2013.

[9] J. Huang, L. Sun, H. Liu et al., "A review on bubble generation and transportation in Venturi-type bubble generators," *Experimental and Computational Multiphase Flow*, vol. 2, no. 3, pp. 123–134, 2020.

[10] S. Khirani, P. Kunwapanitchakul, F. Augier, C. Guigui, P. Guiraud, and G. Hébrard, "Microbubble generation through porous membrane under aqueous or organic liquid shear flow," *Industrial & Engineering Chemistry Research*, vol. 51, no. 4, pp. 1997–2009, 2012.

[11] Y. Achaoui, K. Metwally, D. Fouan et al., "Tunable microbubble generator using electrolysis and ultrasound," *AIP Advances*, vol. 7, no. 1, p. 15011, 2017.

[12] K. Terasaka and H. Tsuge, "Bubble formation under constant-flow conditions," *Chemical Engineering Science*, vol. 48, no. 19, pp. 3417–3422, 1993.

[13] Y. Maeda, S. Hosokawa, Y. Baba, A. Tomiyama, and Y. Ito, "Generation mechanism of micro-bubbles in a pressurized dissolution method," *Experimental Thermal and Fluid Science*, vol. 60, pp. 201–207, 2015.

[14] K. Sato, "Controllable air-bubbles size generator performance with swirl flow," *King Mongkut's University of Technology North Bangkok International Journal of Applied Science and Technology*, vol. 8, no. 4, pp. 245–249, 2015.

[15] M. Takahashi, T. Kawamura, Y. Yamamoto, H. Ohnari, S. Himuro, and H. Shakutsui, "Effect of shrinking microbubble on gas hydrate formation," *The Journal of Physical Chemistry B*, vol. 107, no. 10, pp. 2171–2173, 2003.

[16] M. Takahashi, "ζ potential of microbubbles in aqueous solutions: electrical properties of the gas− water interface," *The Journal of Physical Chemistry B*, vol. 109, no. 46, pp. 21858–21864, 2005.

[17] X. Xu, X. Ge, Y. Qian, B. Zhang, H. Wang, and Q. Yang, "Effect of nozzle diameter on bubble generation with gas self-suction through swirling flow," *Chemical Engineering Research and Design*, vol. 138, pp. 13–20, 2018.

[18] H. S. Alam, A. T. Sugiarto, and G. G. Redhyka, "Unsteady numerical simulation of gas-liquid flow in dual chamber microbubble generator," in *Proceedings of the 2nd International Conference on Automation, Cognitive Science, Optics, Micro Electro-Mechanical System, and Information Technology (ICACOMIT)*, pp. 133–137, IEEE, Jakarta, Indonesia, October 2017.

[19] H. S. Alam, G. G. Redhyka, A. T. S. Bahrudin, T. I. Salim, and I. Robbihi, "Design and performance of swirl flow microbubble generator," *International Journal of Engineering & Technology*, vol. 7, no. 4, pp. 66–69, 2018.

[20] Comsol, "Multiphysics® 5.3 release highlights," https://www.comsol.com/release/5.3/cfd-module.

[21] K. Zhang, Y. Li, Q. Chen, and P. Lin, "Numerical study on the rising motion of bubbles near the wall," *Applied Sciences*, vol. 11, no. 22, Article ID 10918, 2021.

[22] W. Thu and D. Ilin, "Modeling pictures of the flow past rough and smooth surfaces in the program comsol multiphysics," in *Proceedings of the 15th International Conference on Optical Methods of Flow Investigation*, IOP Publishing, Moscow, Russia, June 2019.

[23] Cfd, "Module user's guide," https://doc.comsol.com/5.3/doc/com.comsol.help.cfd/CFDModuleUsersGuide.pdf.

[24] K. Tabei, S. Haruyama, S. Yamaguchi, H. Shirai, and F. Takakusagi, "Study of micro bubble generation by a swirl jet (Measurement of bubble distribution by light transmission and characteristics of generation bubbles)," *Journal of Environment and Engineering*, vol. 2, no. 1, pp. 172–182, 2007.

[25] J. S. Cornejo Caceres, N. Prieto, G. Gonzalez, and A. Chaves-Guerrero, "Numerical simulation of a natural gas cylindrical cyclone separator using computational fluid dynamics," *Industrial & Engineering Chemistry Research*, vol. 58, no. 31, pp. 14323–14332, 2019.

[26] G. Patra, S. Chakraborty, and B. Meikap, "Role of vortex finder depth on pressure drop and performance efficiency in a ribbed hydrocyclone," *South African Journal of Chemical Engineering*, vol. 25, no. 1, pp. 103–109, 2018.

[27] M. Durango-Cogollo, J. Garcia-Bravo, B. Newell, and A. Gonzalez-Mancera, "CFD modeling of hydrocyclones—a study of efficiency of hydrodynamic reservoirs," *Fluid*, vol. 5, no. 3, p. 118, 2020.